



# Optimizing metal grating back reflectors for III-V-on-silicon multijunction solar cells

PETER TILLMANN,<sup>1,2</sup>  BENEDIKT BLÄSI,<sup>3</sup>  SVEN BURGER,<sup>2,4</sup>   
MARTIN HAMMERSCHMIDT,<sup>2,4</sup> OLIVER HÖHN,<sup>3</sup>  CHRISTIANE  
BECKER,<sup>1</sup>  AND KLAUS JÄGER<sup>1,2,\*</sup> 

<sup>1</sup>*Dept. Optics for Solar Energy, Helmholtz-Zentrum Berlin für Materialien und Energie, Albert-Einstein-Straße 16, 12489 Berlin, Germany*

<sup>2</sup>*Computational Nano Optics, Zuse Institute Berlin, Takustraße 7, 14195 Berlin, Germany*

<sup>3</sup>*Fraunhofer Institute for Solar Energy Systems ISE; Heidenhofstr. 2, 79110 Freiburg, Germany*

<sup>4</sup>*JCMwave GmbH, 14050 Berlin, Germany*

\*[klaus.jaeger@helmholtz-berlin.de](mailto:klaus.jaeger@helmholtz-berlin.de)

**Abstract:** Multi-junction solar cells allow to utilize sunlight more effectively than single junction solar cells. In this work, we present optical simulations of III-V-on-silicon solar cells with a metal grating at the back, which experimentally have reached more than 33% power conversion efficiency. First, we perform simulations with the finite element method and compare them with experimental data to validate our model. We find that accurately modeling the investigated geometrical structure is necessary for best agreement between simulation and experimental measurements. Then, we optimize the grating for maximized light trapping using a computationally efficient Bayesian optimization algorithm. The photo current density of the limiting silicon bottom cell is improved from 13.48 mA/cm<sup>2</sup> for the experimental grating to 13.85 mA/cm<sup>2</sup> for the optimized metal grating. Investigation of all geometrical optimization parameters of the grating (period, height, . . .) shows that the structure is most sensitive towards the period, a parameter highly controllable in manufacturing by inference lithography. The results show a pathway to exceed the current world record efficiency of the III-V-on-silicon solar cell technology.

Published by The Optical Society under the terms of the [Creative Commons Attribution 4.0 License](https://creativecommons.org/licenses/by/4.0/). Further distribution of this work must maintain attribution to the author(s) and the published article's title, journal citation, and DOI.

## 1. Introduction

The power conversion efficiency of single-junction silicon solar cells is limited to around 29.4% [1]. With the record efficiency of 26.7% [2] there is little room for improvement. The most substantial factor in the limited conversion is the poor utilization of the solar spectrum. The high energy of short-wavelength radiation is only partially utilized by a silicon semiconductor while a large fraction is lost by thermalization. Combining multiple semiconductors in a multijunction solar cell substantially increases the possible efficiency to 49.8% [3] when using a silicon subcell in a triple junction solar cell.

Cariou *et al.* demonstrated a III-V-on-silicon triple junction solar cell with a power conversion efficiency (PCE) of 31.4% and all planar interfaces [4]. The cell was produced by wafer bonding of a epitaxial grown III-V tandem solar cell with a tunnel-oxide passivated contacts (TOPCon) silicon solar cell. The electrical properties of the cell were excellent, however the absorption of IR light was low because silicon is only weakly absorbing between 1000 nm and 1200 nm.

Light management is important to maximize the absorption of incident light in solar cells. Random pyramid-shaped structures are the industrial standard for silicon solar cells and can often be utilized for silicon-based multi-junction solar cells as well [5]. The pyramids prolong the

average light path in the solar cell and therefore increase the absorption in the weakly absorbing regime of silicon, which is called light trapping.

However TOPCon passivation is not compatible with the standard process for random pyramid texturing. Instead, Cariou *et al.* introduced a square-shaped metal grating back reflector fabricated by nano-imprint lithography. This back reflector allowed them to significantly increase the absorbed photocurrent density in the silicon subcell while retaining the excellent passivation properties of the TOPCon. The triple junction solar cell yielded 33.3% PCE [4]. A record at that time, it was meanwhile improved PCE values exceeding 34% [6].

Metal gratings as light-trapping textures were first proposed by Kiess and Morf [7] and more recent studies demonstrated their applicability in highly efficient silicon solar cells [8–10]. Peters *et al.* investigated the influence of the grating geometry on the performance gain of the metal grating [11]. Further, Cordaro *et al.* investigated silver nano-discs in a hexagonal lattice as back reflectors in III-V-on-silicon cells [12].

Metal gratings deflect a fraction of the light, which reaches the back of the solar cell, away from the zeroth reflection order. If the period of the diffraction grating is shorter than the vacuum wavelength, the diffracted light experiences total internal reflection at the front side of the solar cell [see Appendix A]. Hence, absorptance of a solar cell can be substantially improved in the weakly absorbing regime.

In this work we optically simulate triple-junction solar cells with back side gratings similar to the layer stack used by Cariou *et al.* We compare our simulated results with EQE and reflectance measurements to validate the model and show the importance of the geometrical details of the textured interface. Then, we use Bayesian optimization to find geometric parameters that maximize the absorbed photocurrent in the silicon subcell. Bayesian optimization is well suited to find a global extremum of functions where no gradient information is available and which require long computation times [13]. It was used for a variety of applications such as robotics [14], hyper-parameter tuning [15], optical systems [16] and solar cells [17–19].

Next, we discuss the sensitivity of the optimized structure towards the parameters and how this might affect an experimental realization. Last, we briefly discuss alternative optimization targets and how these might effect the final performance of a solar cell with a metal grating as back reflector.

## 2. Modelling optical response of the solar cell with metal grating back reflector

In this section we explain our simulation approach in detail and show results for solar cells with a planar silicon-silver interface and with two different geometrical models of the textured interface. We compare our results with external quantum efficiency (EQE) and reflectance measurements and discuss the importance of the modeling details for the textured interface.

### 2.1. Investigated setup

Figure 1(a) shows a schematic illustration of the solar cell stack simulated in our work. The solar cell consists of three junctions. The upper two junctions are based on direct bandgap materials (GaInP and GaAs) produced by epitaxial growth on the front. These two junctions are combined with a silicon subcell by wafer-bonding. A silver contact is evaporated onto the back of the solar cell that also acts as a reflector for weakly absorbed infrared light.

In a second setup Cariou *et al.* implemented a textured metal grating as back contact. The grating was prepared by nano-imprint lithography (NIL). For the preparation, SU8 photoresist [20] was spin coated onto the poly-Si contact at the back. The photoresist was UV cured after texturing with a PDMS stamp, replicated from a master created by interference lithography [21]. The surface was then treated by reactive ion etching to remove any photoresist between the structures. Finally the grating resulted from filling the gaps of the photoresist with evaporated

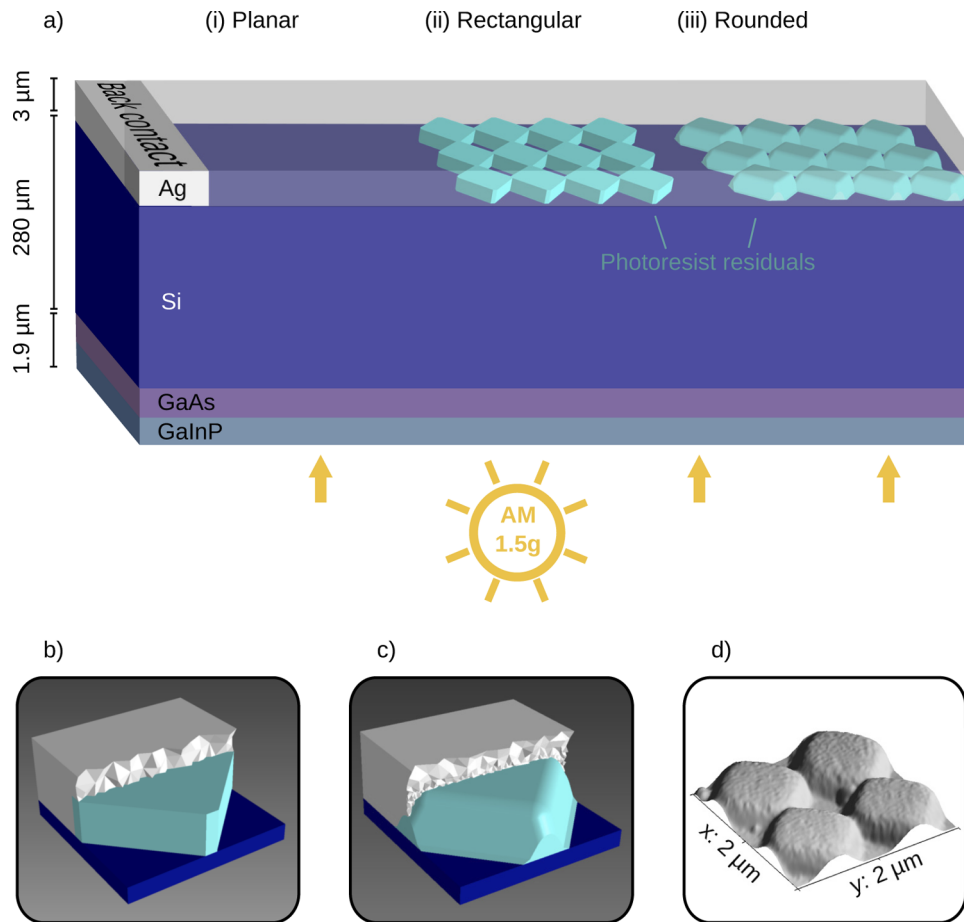


**Fig. 1. Layer stack and interface structures of the optical system.** (a) Schematic illustration of triple junction solar cell stack with three different Si-Ag interface configurations: (i) without periodic grating (planar interface), (ii) idealized grating with rectangular shaped photoresist residuals, (iii) more realistic grating with rounded photoresist residuals. The stack is shown upside down and the incident of the illumination is at the bottom. The rectangular and rounded structures are both used to model the photoresist residuals that remain after nano imprint lithography texturing at the backside of the silicon cell. Mesh grid of the rectangular (b) and round (c) structure as used in the simulation software. (d) Atomic force microscope image of the experimentally implemented grating after NIL patterning of the photo resist before metal evaporation. In the planar samples no photoresist is used in the production process. For more details of the solar cell stack please refer to [4].

silver. Figure 1(d) shows an atomic force microscope image of the surface after texturing the photoresist before the metal contact is evaporated.

Two different model structures are used to simulate the textured solar cell. The rectangular structure shown in Fig. 1(b) is modeled with rectangular side walls (with respect to the base) and approximates the photoresist by intersecting cuboids. This approach is similar to other simulation studies on metal gratings for solar cell applications [22,23]. Reducing the complexity of the texture to cuboids can be necessary because of limitations of the used optical simulation method and might be chosen for ease of implementation. However, this simplification neglects several features of the experimental structure that are visible in electron microscopy images:

- The sidewalls of the photoresist residuals are not perpendicular but have an angle of around  $65^\circ$  between the sidewall and the silicon base.
- Edges and vertices are not sharp but rounded.
- The point of intersection between the cuboid elements is lowered compared to the flat top area.

The rounded structure shown in Fig. 1(c) represents the experimental implemented texture as close as possible. The period of both grating models is 1000 nm and the photoresist structure has a height of 250 nm. The edge length of the cuboid in the rectangular structure is 760 nm. The photoresist residual in the rounded model has a length of 870 nm at the base and 650 nm at the top, resulting in a sidewall angle of around  $65^\circ$ . The edges and vertices of the photoresist block were rounded with a radius of 50 nm, where applicable. All parameters for the simulated geometries were estimated from SEM images.

## 2.2. Numerical simulation of the absorption profile

For simulating the absorption and, subsequently, the absorbed photocurrent density under normal incident AM1.5g [24] illumination we divide the multijunction solar cell stack into three sections.

The transmission, reflection and absorption spectra of the anti-reflective coating, GaInP and GaAs junction, bonding layer and interface to the silicon wafer were previously simulated using a coherent transfer matrix method (TMM) [25]. Due to intellectual property concerns the exact details of the this top layer stack cannot be disclosed.

The absorption in the silicon wafer is calculated with the Beer-Lambert law. The top and bottom silicon tunnel passivated contacts and the polysilicon layers are not considered, instead, the silicon cell is treated as a homogeneous layer.

For modeling of the backside grating we use the finite element method (FEM) software JCMsuite [26]. The optical response was simulated between 950 nm and 1200 nm with a resolution of 10 nm. Below 950 nm almost all light is absorbed in one of the junctions and does not reach the back of the cell.

For computational efficiency, the optical response of the grating is computed for all sources belonging to the same Bloch group [27] in a single simulation. Because the grating is the only non-planar interface in the solar cell stack all diffracted light will remain within orders of the same Bloch group. Consequently, in order to simulate the optical response of the complete solar cell stack only one FEM simulation is required per simulated wavelength. From the FEM Simulation the full scattering matrix of the metal grating is obtained. The scattering matrix connects each incoming to each outgoing diffraction channel. The individual interaction, that takes  $s$  and  $p$  polarization into account, can be described by a Jones matrix with 4 elements. The full scattering matrix (for one wavelength) therefore consists of  $4N \times N$  elements, where  $N$  is the number of propagating diffraction orders. Each interaction with the metal grating redistributes the propagating light into the individual channels of the diffraction orders. Between interactions of the metal grating the absorption of light in the silicon wafer (according to Beer-Lambert law)

and potential transmission and absorption losses in the front layers (from TMM simulation) are calculated. The final result for each wavelength is an absorptance in silicon, parasitic absorptance in the metal and front layers and reflection loss. More details on such formalisms are given in Ref. [28].

From the absorption profile of the three active junctions we calculate the photocurrent. Due to the excellent electric properties of the Si subcell we assume a collection probability of 100%. Therefore the photocurrent in the  $i$ -th subcells is given by

$$J_{\text{ph},i} = e \int_{300 \text{ nm}}^{1200 \text{ nm}} A_i(\lambda) \Phi_{\text{AM 1.5g}}(\lambda) d\lambda \quad (1)$$

with  $e$  as elementary charge,  $A_i(\lambda)$  as the wavelength dependent absorption in the  $i$ -th layer and  $\Phi_{\text{AM 1.5g}}(\lambda)$  as spectral photon flux under AM 1.5g illumination.

### 2.3. Model validation by comparing experimental and simulated solar cell performance

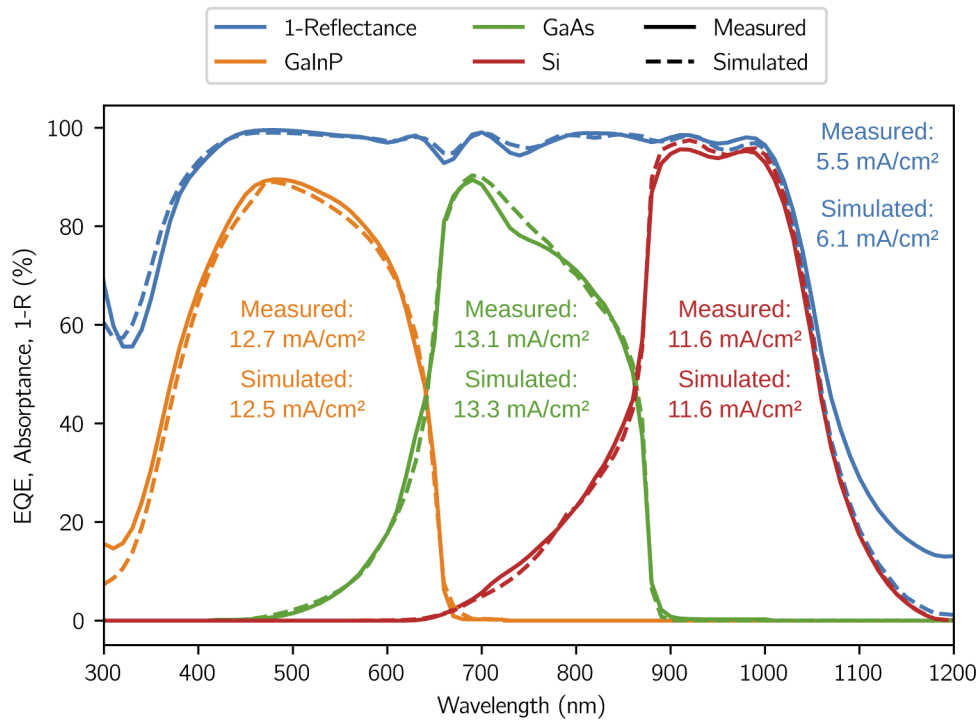
In order to validate our simulation model, we first compare the simulated absorption profiles with experimental external quantum efficiency (EQE) of a fully planar GaInP/GaAs/Si triple junction solar cell device (Fig. 2). To compensate the shading from front contact fingers the incidence light is reduced by 1% for the calculation of the simulated absorption profile. Due to the high reflectivity of the silver front contact fingers 1% of the illumination is added to the simulated reflectance. We assume a collection probability of 100%, allowing us to directly compare measured EQE and simulated absorption profiles.

Experiment and simulation of EQE and absorptance show a very good agreement with only minor deviations in the UV ( $< 350 \text{ nm}$ ) and around  $750 \text{ nm}$ . The reflection also shows good agreement over a wide range of the spectrum, however above  $1000 \text{ nm}$  an overestimation is visible in the simulation. A possible explanation is parasitic absorption in the n-doped polysilicon of the selective top contact, which is not considered in the TMM layer stack. The parasitic absorption in the polysilicon of the selective contact is typically most relevant for wavelength regions below  $500 \text{ nm}$ . However, for strongly doped layers the absorption can increase above  $1000 \text{ nm}$  due to free carrier absorption and can accumulate to several hundred  $\text{nA/cm}^2$  current density [29].

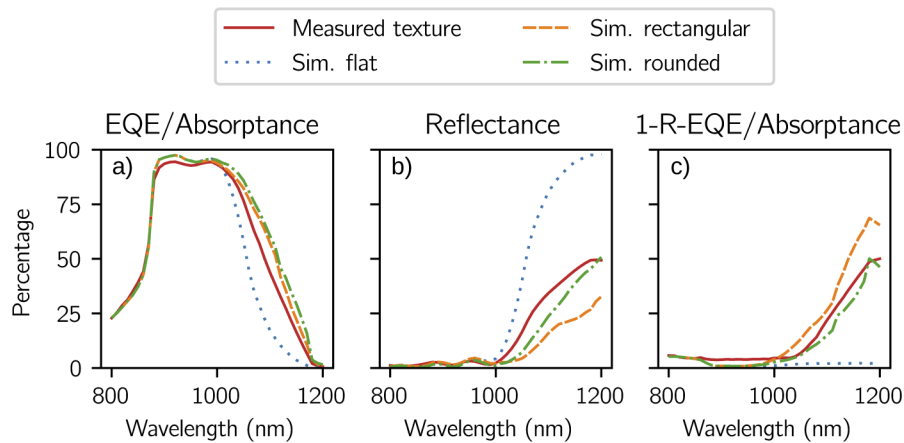
The best planar triple-junction solar cells reached a power conversion efficiency of 31.4% under standard test conditions (STC). The Si junction absorbs a photocurrent density of  $11.6 \text{ mA/cm}^2$  which is significantly less compared to the GaInP and GaAs with  $12.7 \text{ mA/cm}^2$  and  $13.1 \text{ mA/cm}^2$ , respectively, and therefore limiting the short-circuit current density of the complete cell to  $11.6 \text{ mA/cm}^2$ . The reflection losses for light above  $1050 \text{ nm}$  are very large, with over 60% at  $1100 \text{ nm}$ , because of the low absorption coefficient of silicon in this wavelength region. Most of the reflected light is not directly reflected at the illuminated side of the solar cell but passes the cell, is reflected at the silver back contact and subsequently leaves the cell at the front.

Figure 3 shows the EQE/absorptance, reflectance and parasitic absorption losses of the measured cell with periodic metal grating as back reflector, and the respective simulations using a planar rear contact, as well as a periodic grids comprised of rectangular and rounded features. Implementing a textured interface at the back side significantly improves the absorption for wavelengths longer than  $1000 \text{ nm}$ . All simulated absorption profiles slightly overestimate around  $900 \text{ nm}$  due to an underestimation of the parasitic absorption in the top layer stack not considered appropriately by the TMM calculation. Moreover, the simulated textures overestimate the absorptance in the range from  $1050$  to  $1150 \text{ nm}$ . The EQE curve of the rectangular texture is very close to the rounded one and slightly closer to the measured EQE of the real device. However, the two simulated textures show significant differences in reflectance and parasitic absorption.

Table 1 shows the photocurrent density of the silicon subcell and the equivalent current density for the reflection and parasitic absorption above  $1000 \text{ nm}$  for simulations and measurements of



**Fig. 2.** Comparison of experiment and simulation for a planar GaInP/GaAs/Si triple junction solar cell (without metal grating). Measured external quantum efficiency (EQE) (solid lines) and modeled absorbance (dashed lines) of the GaInP, GaAs and Si subcells in the triple junction device with planar rear side, as well as  $(1 - R)$  of the whole device. For the simulated absorbance and reflectance we compensate 1% shading arising from contact fingers at the sun-facing front side of the device.



**Fig. 3.** Comparing simulation and measurement results of the textured cell with planar simulation as reference. (a) EQE measurement and simulated absorbance of the silicon subcell, as well as (b) reflectance ( $R$ ) and (c) parasitic absorption (calculated from  $1 - R - \text{EQE}/\text{absorbance}$ ) of the GaInP/GaAs/Si triple junction solar cell with periodic grating at the rear side. The solid line represents data from the measured cell, dashed and dotted lines show results from simulations.

the textured and planar cells. For the simulated cells the difference to the experimental result is shown in brackets.

**Table 1. Overview of experimental and simulation results for the photocurrent density of the Si-junction  $J_{ph}$ , reflection  $J_{ph, refl}$  and parasitic absorption  $J_{ph, para}$ . Reflection and parasitic absorption are integrated for wavelengths from 1000 nm to 1200 nm to highlight the effect of the metal grating. For the simulated results the differences compared to the experimental results are shown in brackets.**

	$J_{ph}$ (mA/cm <sup>2</sup> )	$J_{ph, refl}$ (mA/cm <sup>2</sup> )	$J_{ph, para}$ (mA/cm <sup>2</sup> )
Planar (Exp)	11.6	4.3	0.9
Planar (Sim)	11.6 (0)	5.0 (+0.7)	0.2 (−0.7)
Texture (Exp)	12.7	2.2	1.7
Rounded texture (Sim)	13.5 (+0.8)	1.7 (−0.5)	1.4 (−0.3)
Rectangular texture (Sim)	13.2 (+0.5)	1.1 (−1.1)	2.3 (+0.6)

The rectangular texture shows a reflectance loss that is about half that of the measured cell with a cumulative reflection of 1.1 mA/cm<sup>2</sup> compared to 2.2 mA/cm<sup>2</sup> for the measured cell. The rounded texture is closer to experiment but still underestimates the reflection by 0.5 mA/cm<sup>2</sup>. The underestimation of reflection is likely due to an overestimation of the diffraction efficiency of the silver grating. In other words, the amount of light that is reflected back into the zeroth order, which can escape from the solar cell stack, is underestimated in the simulations.

The simulated absorption profiles of the rounded and rectangular texture are close to each other because the rectangular texture partially compensates the strong underestimation in reflectance by overestimating the parasitic absorption. While the parasitic absorption is slightly underestimated in the rounded simulation with a differences of −0.3 mA/cm<sup>2</sup> compared to the measurement, the rectangular model shows an overestimation of 0.6 mA/cm<sup>2</sup>.

In summary, in terms of absorptance the rounded and rectangular models perform very similar but a more detailed analysis of reflectance and parasitic absorption shows significant differences and a better agreement between rounded model and experimental measurements. These results highlight the importance of accurately modeling the scattering geometry. There are several possible explanations for the difference in absorption, reflectance and parasitic absorption between the rounded model and the experimental cell: The experimental cell has a micro-rough interface between photoresist and silver that is not present in the model. It seems plausible that this roughness could introduce additional parasitic absorption and decrease the resulting EQE. However, Hauser *et al.* showed with an identical structure that a different etching process yielding very smooth surfaces does not change the EQE [30]. Another possible explanation is the uncertainty of the refractive index data for silver. Published datasets show significant differences in the wavelength region of 1000 nm even so they are determined using planar interfaces [31]. Evaporating silver onto a micro-structured substrate might introduce additional uncertainties on the optical properties of the resulting film.

### 3. Optimizing the metal grating back reflector

As discussed above, the metal grating implemented by Cariou *et al.* significantly increased the absorbed photocurrent density in the silicon subcell from 11.6 to 12.7 mA/cm<sup>2</sup>, improving the overall power conversion efficiency from 31.4% to 33.3%. The grating showed high diffraction efficiency (defined as the fraction of the light diffracted into non-zero orders) without degrading the excellent passivating properties of the contact layers [25]. However, two major loss mechanisms limit the quantum efficiency, when a metallic diffraction grating is used as backside reflector. First, on every interaction with the grating a certain fraction of light will be parasitically absorbed by the metal. Second, another fraction of the light will be redirected into the zeroth order and

can subsequently leave the solar cell at the front side. For a high-performance grating the amount of parasitic absorption in the metal and the escape of light through the zeroth order channel must be minimal. The following optimization aims at finding a grating geometry, where these losses are minimized.

Based on the rounded structure introduced in Section 2., we simultaneously optimized four geometrical parameters to maximize the absorbed photocurrent density in the silicon junction using a Bayesian optimization algorithm [32]. The choice of an optimal optimization algorithm strongly depends on the underlying problem. While Bayesian optimization is often regarded as highly efficient in terms of needed function evaluations [33] different benchmarking studies showed mixed results when compared to other global optimization procedures [34,35]. However, a study by Schneider *et al.* found that Bayesian optimization was highly suitable for numerical optimization of nano-optical systems and significantly outperformed particle swarm, differential evolution and downhill simplex in each investigated setup [32].

In principle, Bayesian optimization consists of two steps: first, an interpolation model approximates the target function and its uncertainty (based on previously evaluated data points). Second, an acquisition function determines the next query point from the interpolation model. After evaluating the function for the queried data point the interpolation model is updated and the next step can be computed with the acquisition function. This cycle is repeated until a specified number of steps or a convergence criterion is reached. The software package for Bayesian optimization provided by JCMSuite was used with a Gaussian process as interpolation model and expected improvement as acquisition function [32].

Table 2 shows the range and constraints of the parameters used to optimize the performance of the silver grating. The bottom width is restricted to be smaller than the period. With increasing size of the bottom width the area of the silicon backside that is covered by the photoresist residuals also increases. However there needs to be a certain contact area between the silicon wafer and the silver back contact. Because of the rotation of  $45^\circ$  between the base of the photoresist residual and the unit cell the minimal contact area between silicon and silver is 17.5% by enforcing that the bottom width is equal or smaller than the period. To prevent an overhanging side wall of the photoresist (to ensure manufacturability) the top width is restricted to be smaller than the bottom width.

**Table 2. Free optimization parameters and their ranges and constraints.**

	Range (nm)	Constraint
Height	100– 500	—
Period	100–1400	—
Bottom Width	100–1400	< Period
Top Width	100–1400	< Bottom Width < Period

The optimization procedure was split into two phases: first, 100 random geometries were simulated to provide an overview of the parameter landscape. This is not strictly necessary for the optimization but can help with the subsequent analysis of the results. Additionally, Bayesian optimization also benefits from knowing random geometries. In the second phase, 400 iterations of Bayesian optimization were performed. Figure 4 shows the FEM unit cell of the experimentally derived configuration (left) and the unit cell of the optimized grating (right). Table 3 shows the parameters and the resulting photocurrent generated in the silicon sub cell of both configurations.

Compared to the experimental structure the optimized version is slightly higher and has a smaller period, a smaller bottom width and a considerably smaller top width. The contact area of the optimized configuration was reduced to about 20% from 30% of the experimental structure due to the changes of bottom width and period. Also the sidewall angle is less steep in the

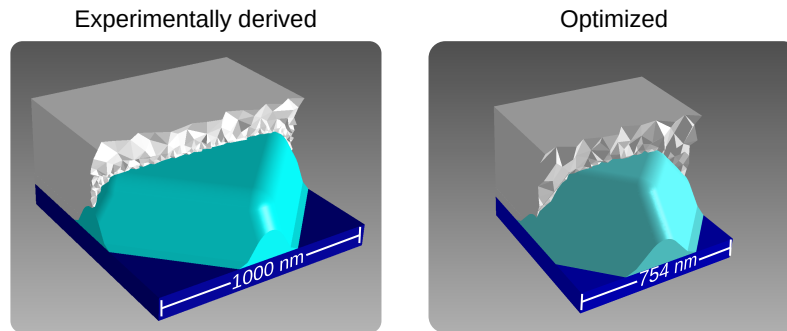


**Fig. 4.** Structure of the FEM unit cell for the simulation of the experimentally derived configuration (left) and the structure yielding the highest photocurrent in the Si junction after optimization.

**Table 3. Parameter range and constraints of the optimization.**

	Height (nm)	Period (nm)	Bottom Width (nm)	Top Width (nm)	Photocurrent density (mA/cm <sup>2</sup> )
Experimentally derived	250	1000	870	650	<b>13.48</b>
Optimized	296	755	740	345	<b>13.86</b>

optimum than in the experimentally derived configuration. Looking from the top onto the unit cell, the area covered by the sidewalls is dominating and only smaller areas are covered by the planar top of the photoresist residual and the silicon-silver interface.

Figure 5 shows the optimization landscape where each of the six hexbin plots represents a combination of two geometrical parameters. Each hexagonal element shows the maximum photocurrent density generated in the silicon subcell and the red star marks the configuration with the highest photocurrent density. Due to the parameter constraints no configuration in the bottom right is sampled for combinations involving bottom width, top width and period because bottom width and top width are restricted to be lower than the period.

Overall, there seems to be a weak interdependence between the different parameters. For combinations of bottom width/height, top width/height, period/height and period/top width choosing one parameter has only small or no effect on the optimal choice of the second parameter. The only pairs showing visible interdependence are top width/height and period/bottom width. The top width/height pair has a negative correlation, resulting in a lower top width with increasing height for optimal combinations. Hence, the structure tends to have a somewhat stable sidewall angle for optimal variations of either top/width or height. On the other hand, period and bottom width are positively correlated. High performing configurations tend to be close to the diagonal, which results in a high covering ratio of photoresist on the silicon wafer. This might even negatively affect the electrical performance of the solar cell due to an increasing series resistance of the back contact resulting from a smaller contact area of the silver with the silicon wafer.

For a period above 1000 nm the gratings are trapping a decreasing fraction of light and in turn the absorbed photocurrent is reduced. In order to trap light diffracted into the first order (or higher) by total internal reflection the period of the grating has to be smaller than the free space wavelength (see Appendix A). Because the backside grating typically strongly diffracts into the first order and the relevant wavelength for light trapping starts above 1000 nm, gratings with a period larger than 1000 nm show low light-trapping performance. Because the parameters top width and bottom width are constraint to be smaller than the period they also lead to weak performance above 1000 nm.

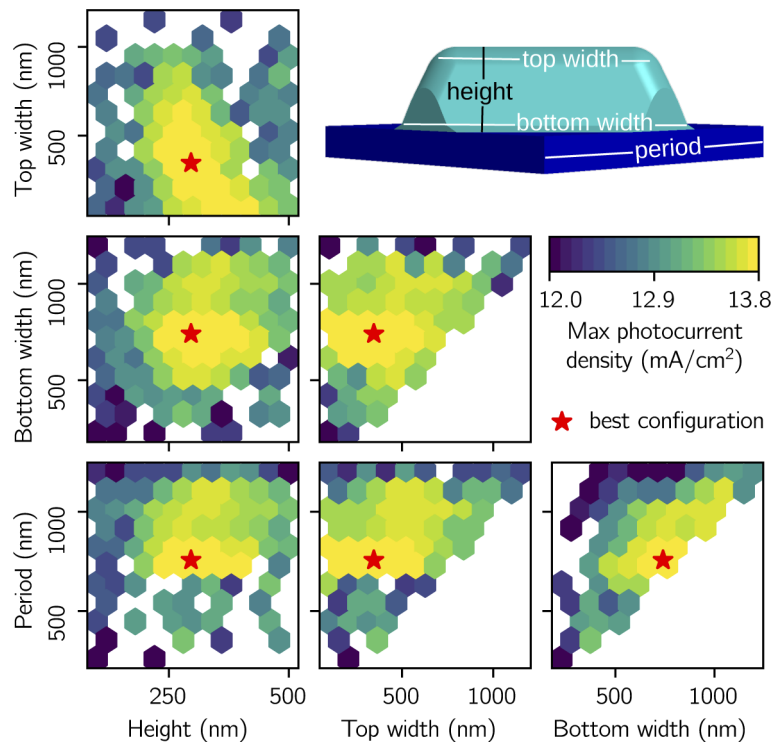


**Fig. 5.** Illustrating the dependence of the photocurrent density on the geometrical parameters and their interdependence for all configurations simulated during the optimization procedure. The six subfigures show each a combination of two parameters where every hexagon represents the maximum photocurrent that was achieved within its extent.

Figure 6 shows the photocurrent density of each configuration as a function of the four geometric parameters. The height shows a broad maximum with very efficient scattering structures for heights between 250 and 350 nm. The top width shows also a broad maximum with an even wider range of 150–500 nm. The period has two distinct sharp maxima, with a local optimum around 1000 nm and the global optimum at around 750 nm. The parameter setting corresponding to the experimental structure by Cariou *et al.* is located in the local maximum of 1000 nm and improvements of the current density might be achieved by switching to a period of 750 nm. The presence of distinct maxima for different periods is similar to results from Peters *et al.* where the height and period of related structures were optimized and local maximum were found around a period of 350 and 730 nm and the global maximum was at 990 nm [11].

To verify the double peak characteristic and exclude the possibility of an optimisation artefact we ran five additional optimizations with a fixed period between 650 and 1050 nm. For each period we performed calculations with 10 random configurations and 40 optimization iterations each. The optimal photocurrent density of these experiments is marked with orange crosses in Fig. 6 d) and confirms the double peak characteristics. The so-found optima lay on top or very close to the existing datapoints of the optimization without constrained period. The datapoint at 950 nm lays in the photocurrent density "valley" between the global maximum at 750 nm and the local maximum at 1050 nm.

The graph for the photocurrent density as a function of the bottom width also shows a double peak, however because the period and the bottom width are not completely independent of each

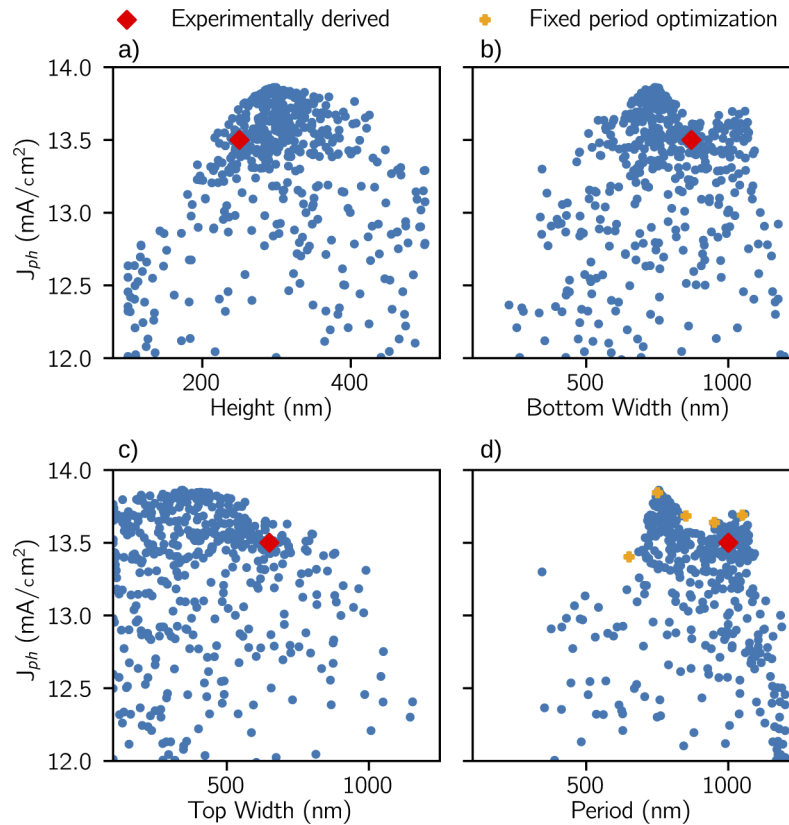


**Fig. 6.** Photocurrent density  $J_{ph}$  generated in the silicon subcell in dependence of the geometric parameters (a) height, (b) bottom width, (c) top width, and (d) period for all configurations simulated during optimization. The red diamond marks the simulation that was performed with the parameters from the experimentally derived configuration. The orange crosses mark the optimum from optimizations with a fixed period.

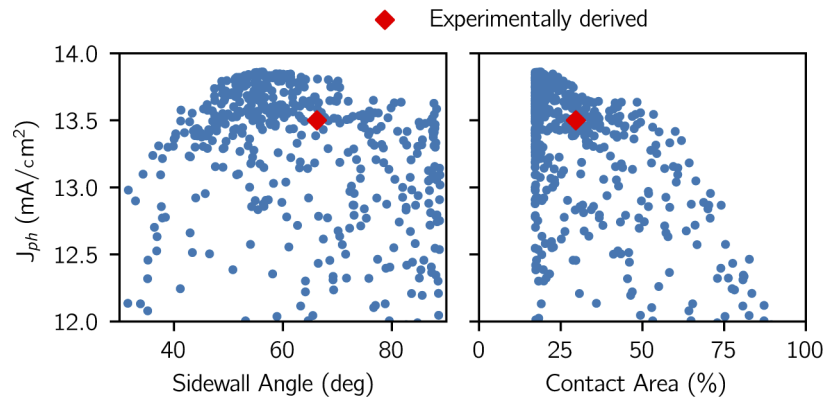
other (the bottom width needs to be smaller than the period) this pattern might just reflect the interdependence between the two parameters as already visible in Fig. 5.

Figure 7 shows scatter plots of the sidewall angle and the contact area, two parameters that can be derived from the other four parameters. Even though the optimized structure shown in Fig. 4 clearly has less steep side walls compared to the experimental structure the side wall angle does not seem to be a critical parameter. This agrees with the broad maximum of the top width. While period and bottom width should be close to 750 nm for optimal performance the top width can be between 150–500 nm without a negative effect on the photocurrent density.

The contact area depends on the ratio of period and bottom width. Because the photocurrent density strongly depends on both these parameters the contact area also shows a narrow maximum at around 20%. In an experimental cell this might have a negative impact on the contact resistance.

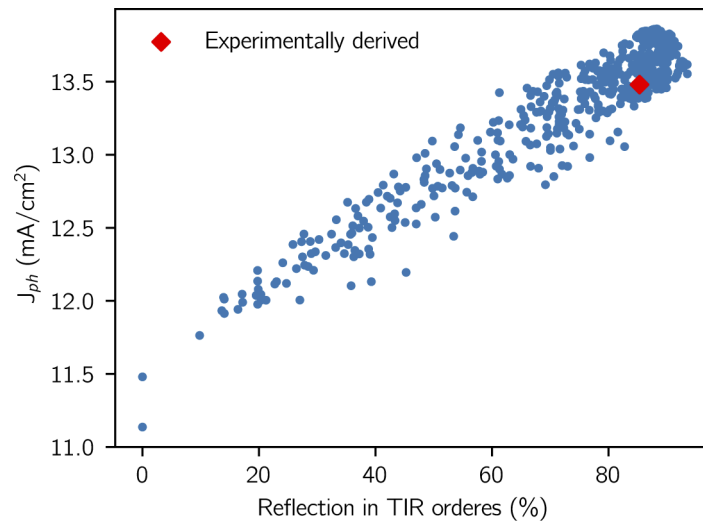
To further analyse the relevant properties that determine the performance of the metal gratings, we investigate the effect of total internal reflection (TIR) of diffracted light. Light diffracted at the backside grating into a non-zero order will often experience TIR (see Appendix A) and therefore its pathway and absorption in the silicon will be increased.

Figure 8 shows the photocurrent density as a function of reflections into TIR orders (averaged over 1000–1200 nm wavelength). The percentage of light directed into TIR orders strongly correlates with the resulting photocurrent density. However, if only configurations with TIR



**Fig. 7.** Photocurrent density  $J_{ph}$  over sidewall angle (a) and electrical contact area between silver back and silicon wafer (b) for all simulated configuration. The red diamond marks the simulation that was performed with the parameters from the experimentally derived configuration.

orders above 80% are considered, the correlation is significantly lower. For reflectance values around 90% a variation of the photocurrent density of around 0.5 mA/cm<sup>2</sup> can be observed. The reason for this is that the light in the TIR orders can be diffracted into an outcoupling direction at further interactions with the grating. Because of the reciprocity of optical systems, the incoupling efficiency for a specific order is equal to its outcoupling efficiency (e.g. if 10% of the light from normal incidence (order zero) is directed into one channel of the first order, 10% of the light incident from that channel will be directed into the zeroth order during the next interaction). If the diffracted light is concentrated into few orders with high efficiency on the first interaction with the grating the same efficiency will apply to out coupling into the zeros order on the second interaction.



**Fig. 8.** Photocurrent density  $J_{ph}$  vs reflection into total internal reflected (TIR) orders for all configuration simulated during optimization. The reflection is averaged over the wavelength range of 1000–1200 nm. The red diamond marks the simulation that was performed with the parameters from the experimentally derived configuration.

Therefore, the reflectance into TIR orders is a suitable parameter to discriminate between good and bad performing metal grating configurations but is not sufficient to distinguish between good and excellent gratings. The metal grating configuration with the highest TIR order reflectance of 94.0% shows a photocurrent density of 13.6 mA/cm<sup>2</sup>, compared to 13.5 mA/cm<sup>2</sup> for the experimentally derived and 13.8 mA/cm<sup>2</sup> for the optimized configuration. If the TIR reflectance were chosen as sole optimization criterion the current gain would have been limited to about one third compared to a full computation of the photocurrent density.

#### 4. Conclusions

In this work, we performed optical simulations of III-V-on-silicon multijunction solar cells with a silver grating at the back. Two main loss mechanisms limiting the light trapping efficiency were identified: parasitic absorption in the silver back contact and back-reflected light escaping through the zeroth-order diffraction. We showed the importance of accurately modeling the used structure to best reproduce the experimental results with optical simulations.

By applying a Bayesian optimization algorithm we optimized the geometric structure of the metal grating to increase the absorbed photocurrent density in the silicon junction—so far the limiting junction of the monolithic triple junction device. The obtained geometrical parameters of the optimized metal grating partly deviated considerably from the initial experimental configuration. In our simulations we were able to improve the photocurrent density from 13.48 mA/cm<sup>2</sup> for the experimentally derived grating geometry to 13.86 mA/cm<sup>2</sup> for the optimized grating. This corresponds to a gain of 0.37 mA/cm<sup>2</sup> or a relative increase of the photocurrent density in the silicon junction by 2.8%.

Further, we analyzed the sensitivity of the optimized metal grating structure with respect to four geometrical parameters: period, height, as well as top and bottom width of the grating features. We found that the period is the most important parameter. From an experimental perspective it is a well controllable parameter.

Finally, we investigated the dependence of the photocurrent density in the silicon subcell on the TIR order reflection of the metal grating. We found a strong correlation. However, to identify high performing metal gratings the TIR order reflection does not suffice.

#### Appendix A — Light trapping by total reflection of diffracted light

The diffractive grating at the back of the solar cell scatters normally incident light away from the interface normal. If the diffraction angle is sufficiently large already light from the first order is trapped by total internal reflection. Figure 9 illustrates the setup and condition for total internal reflection, which is present, when the period of the grating is larger than the vacuum wavelength of the illuminating light. This relationship can be derived by combining the critical angle for total reflection, which is derived from Snell's law of refraction, with the formula for constructive interference at a grating. The constructive interference of the propagating light in the silicon media of the wafer is given by

$$m \frac{\lambda_{\text{Air}}}{n_{\text{Si}}} = m \lambda_{\text{Si}} = d \sin(\theta_d) \quad (2)$$

with  $m$  as reflection order,  $\lambda$  as wavelength,  $n$  as refractive index,  $d$  as the lattice constant and  $\theta_d$  as the diffraction angle. The critical angle for total refraction from the silicon wafer into the air above the cell is given by

$$\sin(\theta_c) = \frac{n_{\text{Air}}}{n_{\text{Si}}} = \frac{1}{n_{\text{Si}}} \quad (3)$$

with  $\theta_c$  as critical angle and  $n$  as refractive index. Combining Eqs. (2) and (3) shows that the diffraction angle  $\theta_d$  is equal to the critical angle  $\theta_c$  for total reflection if the free space wavelength

$\lambda$  is equal to the lattice constant  $d$ .

$$m = 1 \Rightarrow \sin(\theta_c) = \frac{d}{\lambda_{Air}} \sin(\theta_d)$$

$$\lambda = d \Rightarrow \sin(\theta_c) = \sin(\theta_d)$$

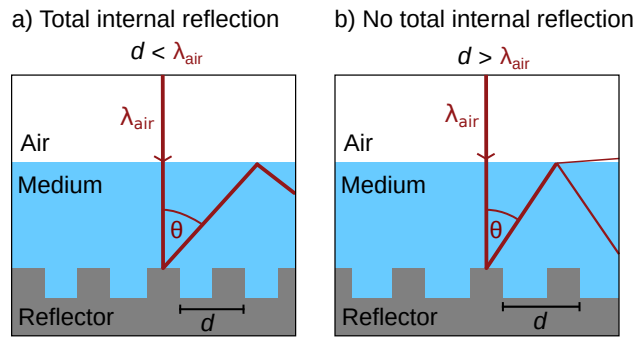


**Fig. 9. Illustrating the trapping of light by total internal reflection.** (a) If the period  $d$  of the metal grating is smaller than the vacuum wavelength first (and higher) order diffracted light will be trapped by total internal reflection. (b) If the period  $d$  of the metal grating is larger than the vacuum wavelength some proportion of the first order diffracted light will escape at the medium/air interface.

**Funding.** Helmholtz Einstein International Berlin Research School in Data Science; Bundesministerium für Wirtschaft und Technologie (0324247); Bundesministerium für Bildung und Forschung (05M20ZBM); Helmholtz Excellence Network SOLARMATH (ExNet-0042-Phase-2-3).

**Acknowledgements.** We thank Philipp-Immanuel Schneider from JCMwave for advice in the implementation and interpretation of Bayesian optimization results. The results were obtained at the Berlin Joint Lab for Optical Simulations for Energy Research (BerOSE) of Helmholtz-Zentrum Berlin für Materialien und Energie, Zuse Institute Berlin, and Freie Universität Berlin.

**Disclosures.** The authors declare no conflict of interest.

**Data availability.** Data underlying the results presented in this paper is available [36]. Python code that allows to generate the figures in this paper from the raw data and recalculate the photocurrent density in the SI junction is available [37].

## References

1. A. Richter, M. Hermle, and S. W. Glunz, "Reassessment of the Limiting Efficiency for Crystalline Silicon Solar Cells," *IEEE J. Photovoltaics* **3**(4), 1184–1191 (2013).
2. K. Yoshikawa, H. Kawasaki, W. Yoshida, T. Irie, K. Konishi, K. Nakano, T. Uto, D. Adachi, M. Kanematsu, H. Uzu, and K. Yamamoto, "Silicon heterojunction solar cell with interdigitated back contacts for a photoconversion efficiency over 26%," *Nat. Energy* **2**(5), 17032 (2017).
3. S. Abdul Hadi, E. A. Fitzgerald, and A. Nayfeh, "Theoretical efficiency limit for a two-terminal multi-junction step-cell using detailed balance method," *J. Appl. Phys.* **119**(7), 073104 (2016).
4. R. Cariou, J. Benick, F. Feldmann, O. Höhn, H. Hauser, P. Beutel, N. Razek, M. Wimplinger, B. Bläsi, D. Lackner, M. Hermle, G. Siefert, S. W. Glunz, A. W. Bett, and F. Dimroth, "III–V-on-silicon solar cells reaching 33% photoconversion efficiency in two-terminal configuration," *Nat. Energy* **3**(4), 326–333 (2018).
5. S. Fan, Z. J. Yu, R. D. Hool, P. Dhingra, W. Weigand, M. Kim, E. D. Ratta, B. D. Li, Y. Sun, Z. C. Holman, and M. L. Lee, "Current-Matched III–V/Si Epitaxial Tandem Solar Cells with 25.0% Efficiency," *Cell Rep. Phys. Sci.* **1**(9), 100208 (2020).
6. S. Glunz, F. Dimroth, M. Hermle, J. Benick, F. Predan, B. Bläsi, A. Fell, A. Richter, H. Hauser, O. Höhn, D. Lackner, P. Schyulla, and R. Müller, "Silicon-Based Monolithic Triple-Junction Solar Cells with Conversion Efficiency >34%," *37th European Photovoltaic Solar Energy Conference and Exhibition* pp. 574–578 (2020).
7. H. Kiess and R. Morf, "Light Trapping In Solar Cells And Determination Of The Absorbed Energy By Calorimetry," in *Optical Materials Technology for Energy Efficiency and Solar Energy Conversion VIII*, vol. 1149 C.-G. Granqvist and C. M. Lampert, eds. (SPIE, 1989), p. 124.

8. J. Eisenlohr, N. Tucher, H. Hauser, M. Graf, J. Benick, B. Bläsi, J. C. Goldschmidt, and M. Hermle, "Efficiency increase of crystalline silicon solar cells with nanoimprinted rear side gratings for enhanced light trapping," *Sol. Energy Mater. Sol. Cells* **155**, 288–293 (2016).
9. B. Bläsi, N. Tucher, J. Eisenlohr, B. G. Lee, J. Benick, H. Hauser, M. Hermle, and J. C. Goldschmidt, "Rear side gratings for silicon solar cells: efficiency enhancement finally demonstrated," in *Photonics for Solar Energy Systems VI*, vol. 9898 R. B. Wehrspohn, A. Gombert, and A. N. Sprafke, eds. (SPIE, 2016), p. 98980A.
10. O. Höhn, H. Hauser, N. Tucher, R. Müller, and B. Bläsi, "Modeling and realization of photonic structures for silicon-based tandem solar cells," in *Physics, Simulation, and Photonic Engineering of Photovoltaic Devices IX*, vol. 11275 A. Freundlich, M. Sugiyama, and S. Collin, eds. (SPIE, 2020), p. 1.
11. M. Peters, M. Rüdiger, H. Hauser, M. Hermle, and B. Bläsi, "Diffractive gratings for crystalline silicon solar cells—optimum parameters and loss mechanisms," *Prog. Photovolt: Res. Appl.* **20**(7), 862–873 (2012).
12. C. E. A. Cordaro, N. Tucher, S. Tabernig, H. Hauser, O. Höhn, R. Müller, B. Bläsi, and A. Polman, "Plasmonic and Mie scattering in nanopatterned back reflectors for III–V-on-silicon solar cells (Conference Presentation)," in *Photonics for Solar Energy Systems VIII*, vol. 11366 J. C. Goldschmidt, A. N. Sprafke, and G. Pandraud, eds. (SPIE, 2020), p. 6.
13. B. Shahriari, K. Swersky, Z. Wang, R. P. Adams, and N. de Freitas, "Taking the Human Out of the Loop: A Review of Bayesian Optimization," *Proc. IEEE* **104**(1), 148–175 (2016).
14. A. Cully, J. Clune, D. Tarapore, and J.-B. Mouret, "Robots that can adapt like animals," *Nature* **521**(7553), 503–507 (2015).
15. J. Snoek, H. Larochelle, and R. P. Adams, "Practical Bayesian Optimization of Machine Learning Algorithms," (2012).
16. P.-I. Schneider, X. G. Santiago, C. Rockstuhl, and S. Burger, "Global optimization of complex optical structures using Bayesian optimization based on Gaussian processes," *Proc. SPIE* **103350**, 103350O (2017).
17. H. C. Herbol, W. Hu, P. Frazier, P. Clancy, and M. Poloczek, "Efficient search of compositional space for hybrid organic–inorganic perovskites via Bayesian optimization," *npj Comput. Mater.* **4**(1), 51 (2018).
18. H. Abdelrahman, F. Berkenkamp, J. Poland, and A. Krause, "Bayesian optimization for maximum power point tracking in photovoltaic power plants," in *2016 European Control Conference, ECC 2016*, (Institute of Electrical and Electronics Engineers Inc., 2017), pp. 2078–2083.
19. P. Tillmann, K. Jäger, and C. Becker, "Minimising levelised cost of electricity of bifacial solar panel arrays using bayesian optimisation," *Sustainable Energy Fuels* **4**(1), 254–264 (2020).
20. J. M. Shaw, J. D. Gelorme, N. C. LaBianca, W. E. Conley, and S. J. Holmes, "Negative photoresists for optical lithography," *IBM J. Res. Dev.* **41**(1.2), 81–94 (1997).
21. A. J. Wolf, H. Hauser, V. Kübler, C. Walk, O. Höhn, and B. Bläsi, "Origination of nano- and microstructures on large areas by interference lithography," in *Microelectronic Engineering*, vol. 98 (Elsevier, 2012), pp. 293–296.
22. A. Mellor, I. Tobías, A. Martí, and A. Luque, "A numerical study of Bi-periodic binary diffraction gratings for solar cell applications," *Sol. Energy Mater. Sol. Cells* **95**(12), 3527–3535 (2011).
23. M. Wellenzohn and R. Hainberger, "Light trapping by backside diffraction gratings in silicon solar cells revisited," *Opt. Express* **20**(S1), A20 (2012).
24. "IEC:60904-3: Photovoltaic devices - Part 3: Measurement principles for terrestrial photovoltaic (PV) solar devices with reference spectral irradiance data," (2008).
25. B. Bläsi, O. Höhn, H. Hauser, R. Cariou, J. Benick, F. Feldmann, P. Beutel, D. Lackner, M. Hermle, G. Siefer, S. W. Glunz, A. W. Bett, F. Dimroth, and N. Tucher, "Photonic structures for III-V//Si multijunction solar cells with efficiency >33%," in *Photonics for Solar Energy Systems VII*, vol. 10688 R. B. Wehrspohn and A. N. Sprafke, eds. (SPIE, 2018), p. 2.
26. J. Pomplun, S. Burger, L. Zschiedrich, and F. Schmidt, "Adaptive finite element method for simulation of optical nano structures," *Phys. Status Solidi B* **244**(10), 3419–3434 (2007).
27. S. Bloch, "Application of the dilogarithm function in algebraic k-theory and algebraic geometry," *Proc. Intern. Symp. on Algebraic Geometry, Kyoto, 1977* (1978).
28. K. Jäger, G. Köppel, M. Hammerschmidt, S. Burger, and C. Becker, "On accurate simulations of thin-film solar cells with a thick glass superstrate," *Opt. Express* **26**(2), A99 (2018).
29. S. Reiter, N. Koper, R. Reineke-Koch, Y. Larionova, M. Turcu, J. Krügener, D. Tetzlaff, T. Wietler, U. Höhne, J. D. Kähler, R. Brendel, and R. Peibst, "Parasitic Absorption in Polycrystalline Si-layers for Carrier-selective Front Junctions," in *Energy Procedia*, vol. 92 (Elsevier Ltd, 2016), pp. 199–204.
30. H. Hauser, O. Höhn, R. Müller, N. Tucher, K. Mühlbach, R. da Silva Freitas, J. Benick, M. Hermle, and B. Bläsi, "Polymer-Based Rear Side Light Trapping Structures for Silicon-Based Tandem Solar Cells," *36th European Photovoltaic Solar Energy Conference and Exhibition* pp. 749–752 (2019).
31. Y. Jiang, S. Pillai, and M. A. Green, "Re-evaluation of literature values of silver optical constants," *Opt. Express* **23**(3), 2133 (2015).
32. P. I. Schneider, X. Garcia Santiago, V. Soltwisch, M. Hammerschmidt, S. Burger, and C. Rockstuhl, "Benchmarking Five Global Optimization Approaches for Nano-optical Shape Optimization and Parameter Reconstruction," *ACS Photonics* **6**(11), 2726–2733 (2019).
33. R. L. Riche and V. Picheny, "Revisiting bayesian optimization in the light of the coco benchmark," (2021). ArXiv: 2103.16649.

34. O. S. Steinholtz, "A Comparative Study of Black-box Optimization Algorithms for Tuning of Hyper-parameters in Deep Neural Networks," Tech. rep., Luleå University of Technology, Department of Engineering Sciences and Mathematics. (2018).
35. T. D. H. D. S. Group, C. Balázs, M. van Beekveld, S. Caron, B. M. Dillon, B. Farmer, A. Fowlie, E. C. Garrido-Merchán, W. Handley, L. Hendriks, G. Jóhannesson, A. Leinweber, J. Mamužić, G. D. Martinez, S. Otten, P. Scott, R. R. de Austri, Z. Searle, B. Stienen, J. Vanschoren, and M. White, "A comparison of optimisation algorithms for high-dimensional particle and astrophysics applications," (2021). ArXiv: 2103.16649.
36. P. Tillmann, B. Bläsi, S. Burger, M. Hammerschmidt, O. Höhn, C. Becker, and K. Jäger, "Data underlying 'Optimizing metal grating back reflectors for III-V-on-silicon multijunction solar cells'," HZB Data Service: 2021, <https://doi.org/10.5442/ND000006>.
37. P. Tillmann, B. Bläsi, S. Burger, M. Hammerschmidt, O. Höhn, C. Becker, and K. Jäger, "Python code reproducing results from 'Optimizing metal grating back reflectors for III-V-on-silicon multijunction solar cells'," Version 1, Zenodo 22 June 2021, <https://doi.org/10.5281/zenodo.5013230>.